Boundary-Layer Meteorol manuscript No.
(will be inserted by the editor)

Interactions between Downslope Flows and a Developing Cold-Air Pool

Paul Burns · **Charles Chemel**

Submitted: 27 November 2013 / Revised: R1 21 May 2014, R2 12 July 2014

Abstract A numerical model has been used to characterize the development of a region of enhanced cooling, in an alpine valley with a width of order 10 km, under decoupled stable conditions. The region of enhanced cooling develops largely as a region of relatively dry air that partitions the valley atmosphere dynamics into two volumes, with air flows partially trapped within the valley by a developing elevated inversion. Complex interactions between the region of enhanced cooling and the downslope flows are quantified. The cooling within the region of enhanced cooling and the elevated inversion is almost equally partitioned between radiative and dynamics effects. By the end of the simulation, the different valley atmosphere regions approach a state of thermal equilibrium with one another, though this can not be said of the valley atmosphere and its external environment.

Keywords Cold-air pools · Downslope flows · Numerical simulation

1 Introduction

Mountain and hill environments (i.e., complex terrain) have been estimated to cover 34 % of Earth's land surface (excluding the Antarctic and Greenland glaciers), directly supporting some 39 % of the growing global human population (Maybeck et al. 2001). Those people not living in these environments may nevertheless partially depend upon them, for example, for a wide range of goods and services including water and energy resources, for biodiversity maintenance, as well as for recreational opportunities (Blyth et al. 2002).

Downslope flows and cold-air pools (CAPs) are well known atmospheric phenomena of complex terrain, particularly under stable decoupled conditions, typical of nocturnal hours

P. Burns
Centre for Atmospheric & Instrumentation Research (CAIR), University of Hertfordshire, College Lane, Hatfield, AL10 9AB, UK

C. Chemel (✉)
National Centre for Atmospheric Science (NCAS), Centre for Atmospheric & Instrumentation Research (CAIR), University of Hertfordshire, College Lane, Hatfield, AL10 9AB, UK
e-mail: c.chemel@herts.ac.uk

and the winter months in sheltered locations. Under these conditions it is known that downslope flows, together with in situ cooling by longwave radiative heat loss to space, control the evolution of CAPs (e.g. Whiteman 2000). In even 'moderate terrain' the temperature variations caused by CAPs can be large. For example, Gustavsson et al. (1998) reported near-surface air temperature variations close to 7 K over horizontal length scales of order 1 km, in terrain with elevation variations less than 100 m. In some places the air temperatures decreased by 8.5 K in 1 h following sunset. Such temperature variations are currently not well represented in weather forecast models (Price et al. 2011), however, they have an important effect on road transport, aviation safety, and agricultural practices (e.g. Price et al. 2011). CAPs must be considered for the effective management of atmospheric pollutants (Anquetin et al. 1999; Brulfert et al. 2005; Chazette et al. 2005; Szintai et al. 2010; Chemel and Burns 2013), and likely have an important modulating effect on climate change estimates (Daly et al. 2010). It is thought that cold-air-pooling processes are capable of affecting the wider atmosphere (Noppel and Fiedler 2002; Price et al. 2011). For the foreseeable future, the representation of the effects of downslope flows and CAPs in both high-resolution forecast models and low-resolution climate and earth-system models, is likely to require varying levels of parametrization, which requires a sound understanding of the underlying physical processes.

Considerable progress has been made at documenting the characteristics of downslope flows and CAPs (see Zardi and Whiteman 2013, for a review, and references therein). However, the two-way interactions between downslope flows and CAPs has so far received little attention. Catalano and Cenedese (2010) used a large-eddy simulation (LES) to carry out a sensitivity study on cold-air pooling within three idealized valleys, which all had a depth of 500 m, and with widths and slope angles ranging between 7 and 13 km, and 5 and 10°, respectively. The depth of the CAP was derived by locating the point along vertical profiles of potential temperature θ, taken through the CAP at different times, which approximately corresponded to the θ-value of a near-neutral profile simulated at sunset. The causes of cooling within and above the CAP were not fully investigated. It was stated that the downslope flows interact with the developing CAP, however, this interaction needs to be further quantified. Burns and Chemel (2014) used a LES to quantify the partitioning of cooling between radiative and dynamics effects (i.e., the combined effects of advection and subgrid-scale mixing), by averaging across the full volume of the valley atmosphere. This paper develops the work of Burns and Chemel (2014) by analyzing the spatial variation of cooling mechanisms within the valley atmosphere, and by considering the complex interactions between the downslope flows and the developing region of enhanced cooling.

The present paper considers cold-air-pooling processes in a valley atmosphere that is not subject to any synoptic forcing, which approximates the case of weak synoptic flows, or where the valley atmosphere is shielded from larger-scale flows by the terrain and possibly by stable layers. The set-up of the model and the design of the numerical simulation are presented in Sect. 2. Numerical results are analyzed in Sect. 3 and a summary is given in Sect. 4.

2 Design of the Numerical Simulation

The numerical simulation presented herein was performed with the Weather Research and Forecasting (WRF) model (Skamarock et al. 2008), version 3.4.1, which is specifically designed for research and operational forecasting on a range of scales. The model set-up used

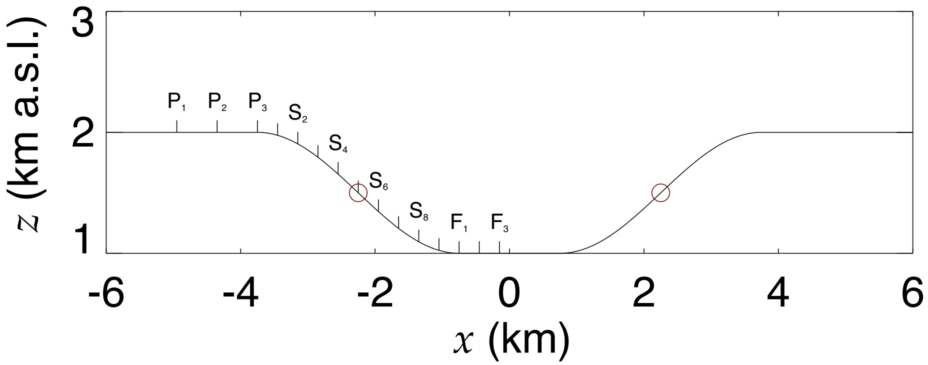

Fig. 1 Variation of terrain height with x, orientated west-east. The terrain is uniform along y (into the page), orientated south-north, though y was given a length of 1.2 km. Symbols adjacent to the ground mark the positions where the downslope flows were analyzed in detail (see Sect. 3). The spacing between the analysis points is constant within each sub-section of the terrain [i.e. plateau (P), slope (S), and valley floor (F)]. The red circles mark the slope inflection points.

for this paper has been described and justified in full by Burns and Chemel (2014). A brief summary of the model set-up is provided here.

An idealized 1 km deep U-shaped valley, with its axis orientated south-north, was implemented with a maximum slope angle of 27.6°, flanked on either side by a horizontal plateau extending 2.25 km from the top of the valley slopes (see Fig. 1). The sinusoidal terrain was made uniform in y, though y was given a length of 1.2 km. The floor of the valley was given a half-width of 750 m and the x-dimension slope length was set to 3000 m. The terrain approximates the environment of the lower Chamonix Valley, located in the French Alps (45.92 °N, 6.87 °E) and all model points were assigned these coordinates.

The model was run in LES mode, with the vertical dry-hydrostatic-pressure coordinate discretized by 101 points. These points were stretched across the vertical coordinate z using a hyperbolic tangent function (Vinokur 1980), which provided a vertical grid resolution Δz of approximately 1.5 m adjacent to the ground. The top of the model domain was set to a height of 12 km above sea level (a.s.l.). The model horizontal grid resolution, $\Delta x = \Delta y$, was set to 30 m, resulting in 402 and 42 points in x and y, respectively. A turbulent kinetic energy 1.5-order closure scheme (Deardorff 1980) was used to model the subgrid scales. The constant C_k in the subgrid-scale parametrization scheme was set to 0.10 (Moeng et al. 2007). Because of the anisotropy of the grid, the width of the filter for the subgrid scales was modified following Scotti et al. (1993) (see also Catalano and Cenedese 2010).

Time integration was performed using a third-order Runge-Kutta scheme using a mode-splitting time integration technique to deal with the acoustic modes. The model time step Δt and acoustic time step were 0.05 and $\Delta t/10$ s, respectively. The parameter β, used to damp vertically propagating sound waves, was set to 0.9 (see Dudhia 1995). Momentum and scalar variables were advected using a fifth-order Weighted Essentially Non-Oscillatory (WENO) scheme with a positive definite filter (Shu 2003), with no artificial diffusion. Earth's rotation effects were neglected.

Model shortwave and longwave radiation physics were represented by the Dudhia (1989) scheme and the Rapid Radiation Transfer Model (RRTM) (see Iacono et al. 2008), respectively. Slope effects on surface solar flux, and slope shadowing effects, were deactivated. The National Severe Storms Laboratory (NSSL) scheme (Mansell et al. 2010) was used to parameterize microphysical processes. The revised MM5 Monin-Obukhov scheme, by Jiménez et al. (2012), simulated the atmospheric-surface layer, which was coupled to the community Noah land-surface model (Chen and Dudhia 2001).

The simulation was provided with an initial weakly-stable linear lapse rate in virtual potential temperature, $\gamma_0 \equiv \partial\theta_v/\partial z|_{t=0} = 1.5\ \mathrm{K\ km^{-1}}$, an environmental lapse rate slightly less than the adiabatic rate. Therefore the simulation represents cases where there is no pre-existing residual layer, or stable layers, in the valley atmosphere at the start of the night, indicative of well-mixed post-convective conditions. The model was run for an 8 h period starting at 1430 UTC on 21 December, that is about 1 h before sunset at the latitude of the Chamonix valley. The atmosphere at the bottom of the valley was assigned an initial $\theta_v = 288$ K, a temperature of about 6 °C. The model skin temperatures T_0 were initialized by extrapolating the first three air temperatures above the ground. A random negative thermal perturbation was added to T_0 with a minimum value of -0.05 K, applied at the initial time across the valley slopes of the domain. The atmosphere was initialized with a constant relative humidity of 40 %, preventing the occurrence of liquid water in the atmosphere. The wind field was zero everywhere at the initial time, simulating decoupled conditions.

The model deep soil temperature, at a depth of 8 m, is denoted T_{deep}. At the bottom of the valley T_{deep} was set to the annual mean surface air temperature of 281.4 K (8.25 °C). T_{deep} was varied with altitude across the idealized terrain at a rate of $-2\ \mathrm{K\ km^{-1}}$. The soil temperature, between the boundary values of T_0 and T_{deep}, was initialized by assuming that $T(z) = c_1 + c_2\, e^{z/d}$, where c_1 and c_2 are constants given the boundary conditions $T(z=0) = T_0$ and $T(z=-3d) = T_{deep}$, where $z \leq 0$. The vegetation and landuse type were set to 'grassland', giving, for winter, a surface albedo of 0.23, a surface emissivity of 0.92, an aerodynamic roughness length of 0.1 m, and a surface moisture availability of 0.3 (volume fraction). The soil type was set to 'silty clay loam', a relatively moist soil (Oke 1987), with dry, wilting point, field capacity and maximum soil moistures of 0.120, 0.120, 0.387 and 0.464 (volume fractions), respectively. The soil was initialized with a constant soil moisture value 10 % below the chosen soil's field capacity, thereby placing the soil within the desired soil water redistribution regime that occurs after soil drainage (Nachabe 1998). The model results therefore consider a soil a few days after rainfall.

The model was run with periodic lateral boundary conditions, with a 4 km deep implicit Rayleigh damping layer (Klemp et al. 2008) implemented at the top of the model domain. The damping coefficient was set to $0.2\ \mathrm{s^{-1}}$.

3 Results and Discussion

The methods used to define the region of enhanced cooling, denoted by CAP_h hereafter, and downslope flows, as well as several other physical regions in and above the valley atmosphere, will first be presented in Sect. 3.1 and 3.2. Each section will end with a broad description of the evolution of the physical features defined therein. The details of the patterns introduced in Sect. 3.1 and 3.2 will be addressed in Sect. 3.3, which requires a consideration of the complex interactions that take place between the CAP_h and downslope flows. The analysis of the system's complexities informs the analysis of its bulk features, which is given in Sect. 3.4. Inevitably, the latter section also informs the analysis of Sect. 3.3.

The subscript h in CAP_h refers to the hydrostatic adjustment made to θ_v in order to reveal the region of enhanced cooling. The CAP_h is evident in the field $\Delta\theta_v \equiv \theta_v - \theta_v\,(t=0)$, where $\theta_v\,(t=0)$ is the hydrostatic variation of θ_v.

3.1 Defining the region of enhanced cooling

This section focuses on defining the CAP_h, however, a number of additional volumes that are useful for the analysis below are also defined. The CAP_h encompasses the ground-based inversion (GBI), which cools significantly more than the rest of the CAP_h, enabling the GBI to be defined within the CAP_h. The growth of the CAP_h is partly controlled by phenomena occurring in volumes close to the top of the valley atmosphere (discussed below), therefore these volumes have also been defined (see Fig. 2a).

The top height of the GBI (z_{GBI}) was tracked by locating the point above the valley floor where $\langle T \rangle_{xy}$ ceased increasing, where T is the air temperature. The averaging operator $\langle \ \rangle_{xy}$ denotes an average across the (x, y) plane, restricted here to the valley floor (i.e. $-0.75 \leq x \leq 0.75$ km). This average is justified by the fact that the iso-surfaces of the model scalar fields are near-horizontal planes above the valley floor (not shown).

In general, the top height of the CAP_h was tracked using both the θ_v field and atmospheric water-vapour mass-mixing ratio field q_v. The accumulated change of θ_v ($\Delta\theta_v$) and the atmospheric stability γ, both averaged across the full y-dimension (denoted by $\langle \Delta\theta_v \rangle_y$ and $\langle \gamma \rangle_y$, respectively) reveal that in general the CAP_h develops with a capping inversion (CI) at its top (see Sect. 3.3.1 for examples of $\langle \gamma \rangle_y$), which can be tracked. For each t the algorithm searched for the maximum $\langle \partial\gamma/\partial z \rangle_{xy}$ above z_{GBI}, thus locating the lower edge of the CI, with this height denoted $z_{CI\downarrow}$. The top of the CI, denoted by $z_{CI\uparrow}$, was then found by searching upwards above $z_{CI\downarrow}$ for the minimum $\langle \partial\gamma/\partial z \rangle_{xy}$. $\langle \Delta\theta_v \rangle_y$ and $\langle q_v \rangle_y$ reveal that in general the CAP_h evolves as a region of relatively dry air surmounted by a thin layer of relatively humid air (not shown). Evidently, the transport of relatively dry air by the downslope flows, from higher altitudes towards the valley floor, is a greater effect than the surface moisture flux, for the model set-up used for this study. The relatively dry downslope flows displace and mix humid parcels adjacent to the valley floor upwards. These humid parcels are forced higher as the valley fills with relatively dry air. The lower edge of the layer of high-q_v air, denoted $z_{HL\downarrow}$, where HL stands for humid-layer, was located by searching above z_{GBI} for the maximum $\langle \partial q_v/\partial z \rangle_{xy}$. The upper edge of the layer ($z_{HL\uparrow}$) was then located by searching upwards above $z_{HL\downarrow}$ for the minimum $\langle \partial^2 q_v/\partial z^2 \rangle_{xy}$.

Soon after $t = 60$ min a narrow region of relatively well-mixed air develops close to the top of each slope and spreads roughly horizontally toward the valley axis. The top and bottom of this layer are denoted by $z_{UML\downarrow}$ and $z_{UML\uparrow}$, respectively, where UML stands for upper mixed layer. This region is characterized by high-shear and vortices and lies directly beneath the region of near-horizontal streamlines, directed from the valley axis towards the plateaux, noted by Burns and Chemel (2014). These features contribute to the development of an elevated inversion and trap air within the valley; they play an important role in the development of the CAP_h (see Sect. 3.3.2).

Throughout the simulation a thin layer of relatively stable air develops above $z_{UML\uparrow}$, where the top of this layer is denoted by $z_{USL\uparrow}$, where USL stands for upper stable layer. The heights defining the UML and USL were defined in essentially the same way as the heights defining the CI and HL.

The curves in Figure 2a compare well with the vertical structure of their corresponding fields away from the valley slopes. Close to the slopes the fields tend to curve upwards away from the horizontal, resulting in some under-estimation of field heights. Intense mixing takes place close to the sloping ground where the downslope flows interact with the dense air of the CAP_h. This can result in the CI being ill defined in this region when it can still be defined further away from the slopes.

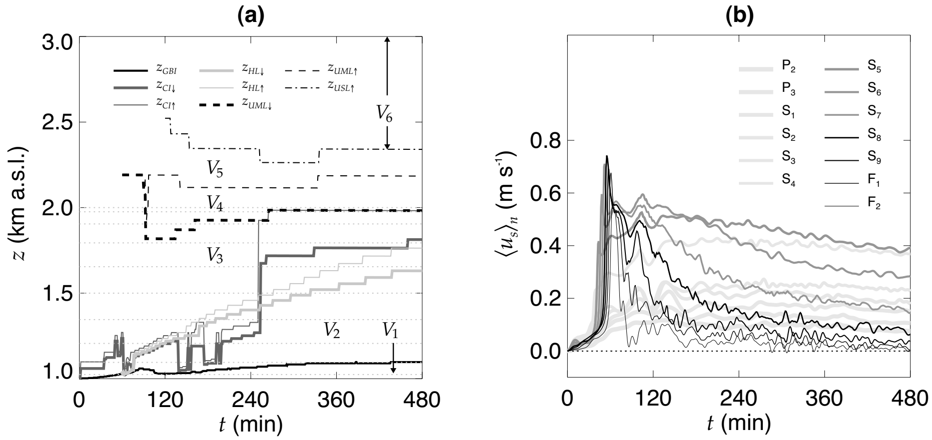

Fig. 2 Time series of **(a)** the height of the ground-based inversion, z_{GBI}, the lower and upper boundaries of the capping inversion (denoted by $z_{CI\downarrow}$ and $z_{CI\uparrow}$, respectively), the humid layer (defined by $z_{HL\downarrow}$ and $z_{HL\uparrow}$), and the upper mixed layer (defined by $z_{UML\downarrow}$ and $z_{UML\uparrow}$). The top edge of the upper stable layer is denoted by $z_{USL\uparrow}$ (see text for details). Horizontal dotted lines mark the heights of the analysis points shown in Fig. 1. Six volumes are defined by $V_1 : 1\text{ km} < z < z_{GBI}$, $V_2 : z_{GBI} < z < z_{HL\downarrow}$, $V_3 : z_{HL\uparrow} < z < z_{UML\downarrow}$, $V_4 : z_{UML\downarrow} < z < z_{UML\uparrow}$, $V_5 : z_{UML\uparrow} < z < z_{USL\uparrow}$, and $V_6 : z_{USL\uparrow} < z < 3$ km. The volumes were limited along x between the top of each slope (i.e. $-3.75 \leq x \leq 3.75$ km) and allowed to encompass the full y-dimension, and **(b)** the layer-averaged downslope flows $\langle u_s \rangle_n$ (defined in Sect. 3.2) at the analysis points defined in Fig. 1. Note that after $t = 180$ min $\langle u_s \rangle_n$ increases from P_2 to S_5 before decreasing between S_5 to F_2.

The curves demarking the CI and HL in Fig. 2a indicate that the CAP$_h$ expands upwards through the valley atmosphere after $t \approx 60$ min. The GBI is also shown to gradually deepen after $t \approx 120$ min. There are a number of complexities in the curves of Fig. 2, for example, there are significant differences in the heights of the curves for the CI and HL after $t = 120$ min. A number of discontinuities exist in the curves for the CI, and the GBI top height includes a maximum point before $t = 120$ min. These complexities are the result of the varying interactions between the downslope flows and developing CAP$_h$, which will be discussed in Sect. 3.3.

3.2 Defining the Downslope Flows

The components of the velocity field $\mathbf{u}$ in WRF are given with respect to the Cartesian coordinate system (x, y, z). By applying an orthogonal transformation to (x, y, z) with rotation/slope angle α, a slope-orientated coordinate system (s, y, n) is introduced, with s directed downslope and n pointing away from the slope. In accord with the usual geometric convention, α is defined to be negative for clockwise rotations, from the line defined by x. The components of $\mathbf{u}$ along s and n, denoted by u_s and u_n, respectively, were obtained from $\langle \mathbf{u}_{xz} \rangle_y$, $\mathbf{u}_{xz} \equiv (u, w)$. The analysis also considers u_s and u_n averaged across the depth of the downslope flows, denoted by $\langle u_s \rangle_n$ and $\langle u_n \rangle_n$, respectively. The upper limit for the average across n (n_{df}) was calculated by searching within 100 m above the ground for the first point where u_s falls below 20 % of its maximum value $u_{s,j}$ (the downslope flow jet speed, located at n_j), that is, where $u_s < c_3\, u_{s,j}$, $c_3 = 0.2$. A 100-m long normal vector was constructed for each x point with a resolution of 1 m, approximately Δz in this region. A more exact estimate of n_{df} where $u_s = c_3\, u_{s,j}$ was then obtained by linear interpolation. The value of c_3

is arbitrary, chosen to avoid any large under- or over-estimations of n_{df}. If $c_3 u_{s,j}$ could not be found, then the n-point associated with the maximum (minimum) $\partial^2 u_s/\partial n^2$ was used for the western (eastern) slope. This latter method focuses on the shape of the downslope flow profile rather than on relative flow speeds. The algorithm, designed for cases with a fairly distinct downslope flow jet, was found to work effectively away from the slope extremities (not shown).

Figure 2b shows $\langle u_s \rangle_n$ for the analysis points P_2 to F_2 defined in Fig. 1. Figure 2b reveals the essential spatial and temporal structure of the y- and n-averaged downslope flow field. The curves for the points over the valley slope reveal the initial propagation of the downslope flow maximum region down the slope, which reaches the valley floor close to $t = 60$ min. Burns and Chemel (2014) demonstrated the presence of an anticyclonic vortex (with rotation axis along y) at the front of this maximum region, which is an example of a microfront, a phenomenon discussed more generally by Mahrt (2014), whom observed them in shallow fog layers. A general increase of $\langle u_s \rangle_n$ is evident moving from the western plateau to the western slope inflection point (S_5), followed by a general decrease of $\langle u_s \rangle_n$ towards the valley floor. One exception is the curve for S_5 before $t \approx 180$ min. A clear increase and decrease of $\langle u_s \rangle_n$ occurs over time for points located below S_3, with the decrease shown to begin earlier in time for points further down the slope. This is consistent with the retreat of the region of maximum downslope flows back up the western slope as the CAP$_h$ expands upwards, noted by Burns and Chemel (2014) and implied by Catalano and Cenedese (2010).

3.3 Co-evolution of the region of enhanced cooling and downslope flows

3.3.1 Initial evolution of the region of enhanced cooling

$\langle \gamma \rangle_y$, and $\langle \Delta\theta_v \rangle_y$ with over-plotted streamlines (as in Fig. 3b), reveal that the CI is first formed soon after $t = 60$ min, when the region of maximum downslope flows reaches the valley floor. At this time the accelerated flows transport cold (low-θ_v) air (relative to the atmosphere away from the ground along x) along the slopes towards the valley floor, and mix it approximately 200 m into the atmosphere, generally increasing γ in this region. These flows also partly mix the pre-existing largely radiatively cooled air-layer, adjacent to the valley floor, higher into the atmosphere, noted by Burns and Chemel (2014). After the intensification of the downslope flows their effect on the CAP$_h$ is more complex. At these later times the downslope flows are comprised of a layer of relatively cold (low-θ_v) air close to the ground, however, the top part of the downslope flows contains relatively warm (high-θ_v) air. The downslope flows advect higher-θ_v air from above that increases $\Delta\theta_v$ in the top part of the downslope flows that is less affected by the cooling surface. Despite this advection of warm air into the CAP$_h$ the downslope flows on average have a cooling effect on the CAP$_h$ (see Sect. 3.4). This is due to both the transport of cold air close to the ground and the bulk rising motions induced to conserve mass, which causes adiabatic cooling.

Figures 2a and 4a show that the intensification of the downslope flows causes both a rapid increase in the depth and a reduction in the intensity or strength (denoted by I_{GBI}), of the GBI between $t = 60$ and 85 min (with z_{GBI} rising from 1026 to 1060 m a.s.l., and I_{GBI} decreasing from 2.64 to 1.50 K), supporting the pattern of mixing stated above.

Mixing from the dynamics creates a relatively well-mixed region within the CAP$_h$, which defines the CI, that is the mixing is non-uniform within the CAP$_h$ (see Fig. 3). Hence, the CI cannot exist before the downslope flow intensification and the curves for $z_{CI\downarrow}$ and $z_{CI\uparrow}$ are difficult to interpret before this event. This intensification of the dry downslope flows dis-

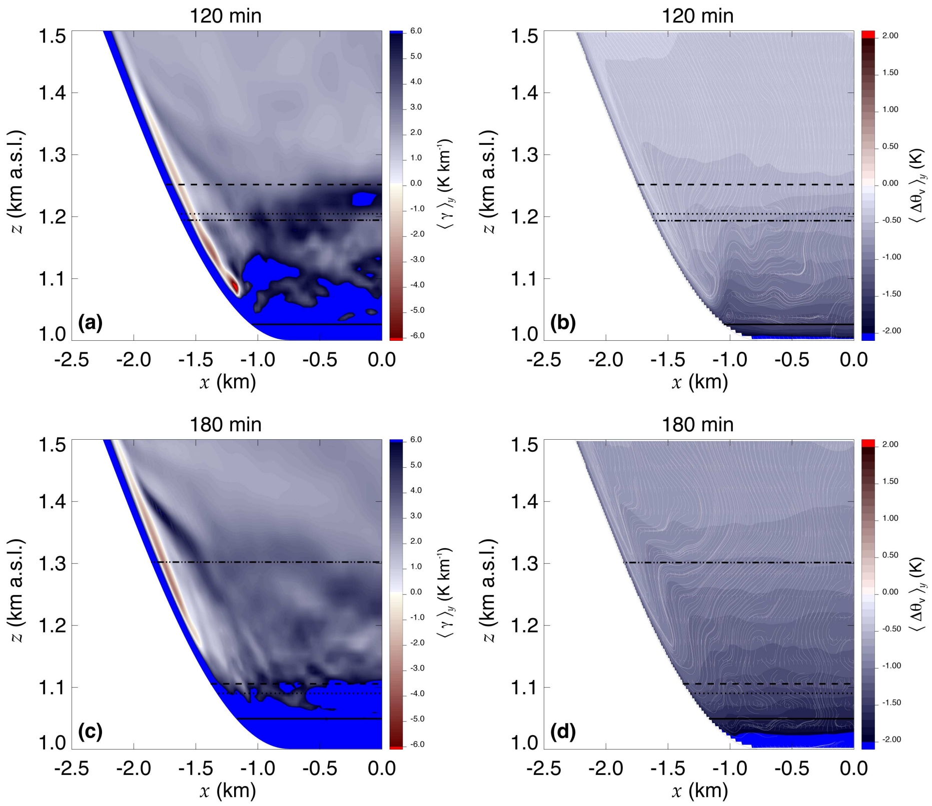

Fig. 3 Contour plots of **(a)** $\partial\theta_v/\partial z$ averaged across the model y-dimension $\langle\gamma\rangle_y$ and **(b)** the accumulated change of θ_v from $t = 0$, averaged across y, $\langle\Delta\theta_v\rangle_y$, with over-plotted streamlines, both at $t = 120$ min, and **(c)** and **(d)** the same type of plots as for **(a)** and **(b)** but at $t = 180$ min. The solid, dashed, dotted and dash-dotted lines mark, respectively, the heights of the near-surface inversion z_{GBI}, the upper and lower boundaries of the capping inversion ($z_{CI\uparrow}$ and $z_{CI\downarrow}$), and the approximate height where the downslope flows are neutrally buoyant. The latter corresponds to $F_b \approx 0$ and is used later in this section. The streamlines were created using $\langle\mathbf{u}_{xz}\rangle_y$, $\mathbf{u}_{xz} \equiv (u, w)$, projected onto a 5-m linear orthogonal mesh, where the resolution of the new grid was justified by Burns and Chemel (2014). The streamlines were seeded on the Cartesian grid, with the same origin, with a resolution of 35 m, which is generally close to the model grid resolution in this region of the atmosphere.

places humid air adjacent to the valley floor upwards. Mixing caused by the downslope flows tends to re-sort parcels according to their moisture content, forcing moist lighter parcels above dry heavier ones. Therefore $z_{HL\downarrow}$ and $z_{HL\uparrow}$ are undefined during the first 60 min of simulation. Despite the difficulty interpreting $z_{CI\downarrow}$ and $z_{CI\uparrow}$ before $t = 60$ min, the algorithm captures the upward displacement of air and the general perturbation of the lower valley atmosphere. This coincides with the initiation of internal gravity waves (IGWs) in and above the valley atmosphere, effects noted by Burns and Chemel (2014).

$\langle\Delta\theta_v\rangle_y$, $\langle\gamma\rangle_y$ and $\langle q_v\rangle_y$ indicate that between $t \approx 70$ and 180 min the CAP$_h$ expands upwards, together with its CI, carrying the layer of relatively high-q_v air to greater heights. Over the same time period mixing processes gradually erode the CI, close to the top of the CAP$_h$, so that by $t \approx 180$ min it is not well defined (compare Fig. 3a and 3c). This is reflected in Fig. 2a by a large sudden decrease in $z_{CI\downarrow}$ and $z_{CI\uparrow}$; at this time the algorithm used to track the CI finds a lower layer of relatively large γ that does not demark the top of the CAP$_h$. After this discontinuity a layer of large γ is found by the algorithm at a lower height range than the CI height range before the discontinuity, but is soon eroded away. A similar behaviour occurs close to $t = 140$ min (discussed below), however, between $t = 140$ and 180 min a CI is present at the top of the CAP$_h$, which can be reasonably estimated by $z_{HL\downarrow}$.

Figure 2a suggests that the early development of the CAP$_h$ erodes away the top of the GBI, decreasing z_{GBI} from a maximum of 1060 m a.s.l. at $t = 85$ min to a minimum of 1026 m a.s.l. at $t = 121$ min. This coincides with the time period when the maximum region of the downslope flows is forced back up the slopes by the CAP$_h$ (see Fig. 4b). Relatively intense mixing close to the front of this maximum region erodes away the top of the GBI (as also indicated by the streamlines in Fig. 3b).

Figure 4b compares $z_{HL\downarrow}$ to a number of downslope flow characteristics in order to investigate some of the interactions between the CAP$_h$ and the downslope flows. The curves denoted by $\max(u_{s,j})$, $\max(\langle u_s \rangle_n)$, and $\max(\langle u_n \rangle_n)$ show the heights corresponding to the greatest $u_{s,j}$, $\langle u_s \rangle_n$ and $\langle u_n \rangle_n$, respectively. These curves show the initial propagation of the downslope flow maximum region down the western slope (matching the patterns in Fig. 2b).

It should be noted that the simulation completed for this work avoided the additional complexity of shadowing effects. This allows the significance of shadowing on the development of cold air pools to be quantified in future work. Shadowing is likely to cause a different initiation of the downslope flows. Nadeau et al. (2012) took observations in an Alpine valley with a roughly similar configuration and orientation to that considered by this work. Near-zero flow speeds were observed close to sunset during what was termed the ‘early-evening calm’ period [see also Acevedo and Fitzjarrald (2001) and Mahrt et al. (2001)]. The initiation of the downslope flows was found to be controlled by the movement of a shading front from the bottom towards the top of the valley slopes.

Between $t \approx 60$ and 180 min it is clear that as the CAP$_h$ top height increases (reasonably estimated by $z_{HL\downarrow}$ during this period) so does the height of $\max\left(\langle u_s \rangle_n\right)$ and $\max\left(u_{s,j}\right)$, which quantifies the initial retreat of the downslope flow maximum region back up the valley slopes. This retreat of the maximum region matches the patterns of decreasing $\langle u_s \rangle_n$ below slope point S_3, noted in Sect. 3.2. Time series of the mass flux computed from the above defined flow speeds show essentially the same patterns as those already discussed.

The sudden decrease of $z_{CI\downarrow}$ and $z_{CI\uparrow}$ at $t \approx 140$ min is associated with the development of a relatively well-mixed layer, immediately above z_{GBI}, with this layer generally expanding upwards over time with the CAP$_h$ (compare Fig. 3a and 3c). Figure 3 indicates that the development of relatively well-mixed regions within the CAP$_h$ are generally associated with regions where $\langle \mathbf{u}_{xz} \rangle_y$ and $\nabla_{xz} \langle \mathbf{u}_{xz} \rangle_y$ are relatively large, where ∇_{xz} is the (x,z) part of ∇. These regions promote both explicit mixing and shear-induced subgrid-scale mixing, where the latter essentially relies on elements of $\nabla\left(\nabla \mathbf{u}\right)$ (see Skamarock et al. 2008). The streamlines give a rough idea of relative flow strengths, so the above observation was confirmed by an analysis of $|\langle \mathbf{u}_{xz} \rangle_y|$ (not shown). An exact correspondence between the stability of the atmosphere, flow strengths and flow gradients is not expected due to the averaging process. It is also not expected that a particular flow configuration will immediately alter the atmospheric stability, which may take time to adjust to the flow regime. The relatively well-mixed regions generally correspond to regions of large $-\langle \mathbf{u}' \cdot \nabla \theta_v' \rangle_y$, the Reynolds stress term for the conservation of energy (not shown), where the perturbations were computed by averaging across y. This is justified by the fact that only small variations of $\mathbf{u}$ occur along y, due to the 2D geometry and near-y-independent thermal forcing at the ground-air interface.

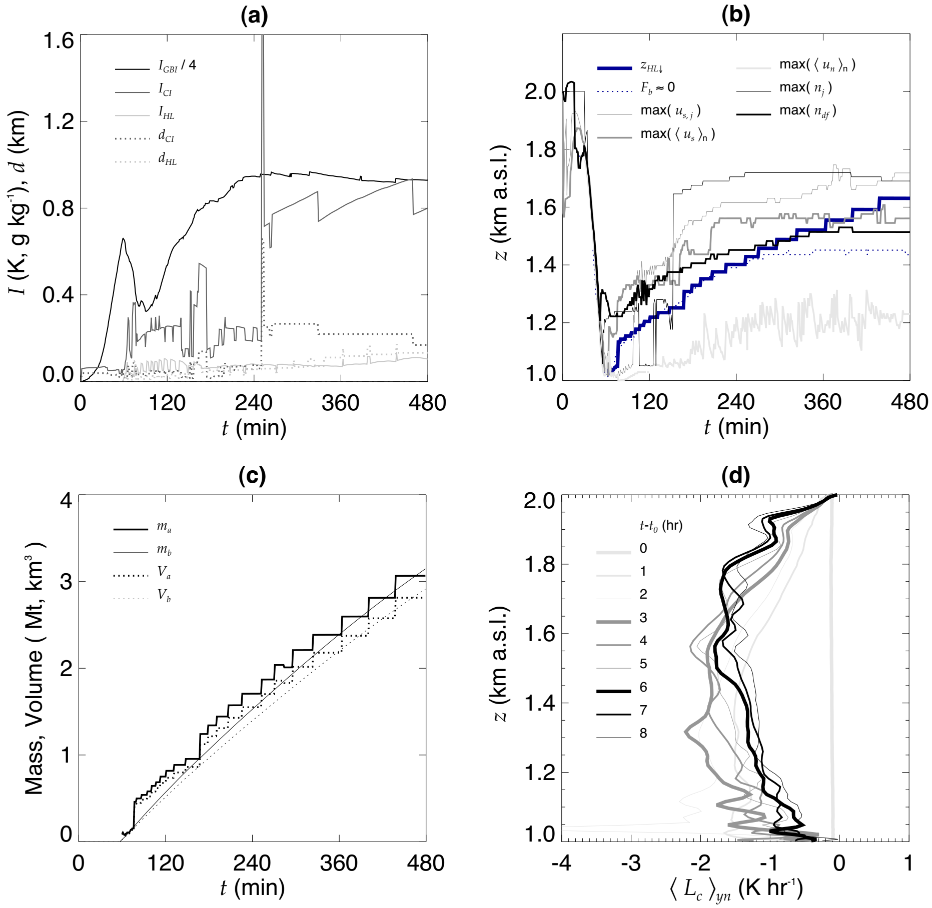

Fig. 4 Time series of **(a)** the intensity (strength) of the ground-based inversion, capping inversion and humid layer, denoted I_{GBI}, I_{CI} and I_{HL}, respectively. I_{GBI} and I_{CI} were defined as the difference in $\langle\theta_v\rangle_{xy}$ across the layers, and I_{HL} as the difference in $\langle q_v\rangle_{xy}$ between the centre and bottom of the layer. The depths of the capping inversion and humid layer are also shown, denoted by d_{CI} and d_{HL}, respectively, **(b)** $z_{HL\downarrow}$ compared against a number of downslope flow characteristics. These include the height of the greatest downslope flow jet speed, denoted by max($u_{s,j}$). The height of the greatest layer-averaged flow along and normal to the slope is denoted by max($\langle u_s\rangle_n$) and max($\langle u_n\rangle_n$), respectively. The height where $u_{s,j}$ is furthest from the ground along n (i.e., the greatest n_j) is denoted by max(n_j). The height where the depth of the downslope flow is greatest is denoted by max(n_{df}). The height where the downslope flows are neutrally buoyant is also provided (i.e., where $F_b \approx 0$), see text for details. **(c)** Time series of the mass and volume of air below $z_{HL\downarrow}$, denoted by m_a and V_a, respectively, and the accumulation of mass and volume, across $z_{HL\downarrow}$, from the downslope flows, denoted by m_b and V_b (see text for details). **(d)** shows the hourly variation with height (by moving along s) of the two-dimensional layer-averaged diabatic cooling rate $\langle L_c\rangle_{yn}$.

$\langle u_n\rangle_n$ approximates the net mass flux along n and so $\max(\langle u_n\rangle_n)$ suggests that detrainment of air from the slopes, considering the resolved flow, reaches a maximum not far above z_{GBI}, which is generally supported by an analysis of the streamlines of $\langle \mathbf{u}_{xz}\rangle_y$ (see Fig. 3).

An analysis of $\langle u_n\rangle_n$ reveals some detrainment of air above $z_{HL\downarrow}$, however, the amount of detrained air in this region is much smaller than below $z_{HL\downarrow}$ (see Fig. 5a). Figure 5a shows the variation of $\langle u_n\rangle_n$ with height (i.e. along s), for $t = 90$, 180 and 300 min. The horizontal dotted-lines correspond to $z_{HL\downarrow}$ at the three different times ($z_{HL\downarrow}$ increases with time). A greater detrainment effect might be expected for a larger γ_0. Below $z_{HL\downarrow}$, multiple maxima and minima of $\langle u_n \rangle_n$ indicates a layering effect as the downslope flows detrain into the valley atmosphere, inducing wind shears and mixing. A similar layering effect was found by Neff and King (1989) who observed the formation of a CAP that grew from the floor of the De Beque Canyon, located along the Colorado River, USA. Reduced entrainment (or slight detrainment) is evident within the elevated inversion, as well as enhanced entrainment below it. This is generally in-line with the analytical theory laid out by Vergeiner and Dreiseitl (1987). This reduction of entrainment or slight detrainment suggests that the elevated inversion helps to shield the valley atmosphere from flows above. The importance of this effect remains unclear. A slight entrainment of air is evident immediately below $z_{HL\downarrow}$ during approximately the last hour of simulation.

Generally detrainment occurs below a level approximately 100 m above $z_{HL\downarrow}$. This detrainment occurs both above and below the height where the downslope flows are neutrally buoyant (i.e., where the buoyancy force $F_b = \langle g\,\theta_v'/\theta_{v_a} \sin\alpha \rangle_n = 0$). F_b is expressed in slope orientated coordinates (as above) for a Boussinesq fluid. g is the acceleration due to Earth's gravitational field, $\theta_v'(s,n,t) = \langle \theta_v \rangle_y - \theta_{v_a}$, is the perturbation from the ambient θ_v-field $\theta_{v_a}(z,t) = \langle \theta_v \rangle_{xy}$, where the averaging operators are those used in Sect. 3.1. The approximation $\rho'/\rho_r \approx -\theta_v'/\theta_{v_a}$ has been used, where ρ' is the perturbation from a constant reference density ρ_r. $F_b \approx 0$ was located by first finding the maximum and minimum F_b, and then searching from the maximum towards the minimum position.

Generally entrainment occurs above a level approximately 100 m above $z_{HL\downarrow}$. These detrainment and entrainment effects are evident in the streamlines of $\langle \mathbf{u}_{xz} \rangle_y$. Significant variations of $-\langle \mathbf{u}' \cdot \nabla\theta_v' \rangle_y$ close to the ground surface essentially mirror the changes of $\langle u_n \rangle_n$. $-\langle \mathbf{u}' \cdot \nabla\theta_v' \rangle_y$ indicates negligible mixing close to the ground surface in the entrainment region but enhanced mixing within about 200 m from the slopes in the detrainment region. Enhanced shear-induced mixing is likely to occur where the downslope flows detrain and where they 'spring-back' after 'over-shooting' $F_b \approx 0$. This region of enhanced shear is evident in the streamlines of $\langle \mathbf{u}_{xz} \rangle_y$ (see Fig. 3). A similar pattern of entrainment and detrainment, as well as the 'spring-back' effect were found by Baines (2008), studying gravity currents flowing down a steep uniform slope in irrotational stratified liquids, in what was termed the 'plume regime'.

The streamlines in Fig. 3 indicate that the thin regions of unstable air above the downslope flows are linked to the return flows associated with the spring-back effect. The return flows transport low-θ_v air from the bottom of the valley. The downslope flows advect higher-θ_v air downslope that increases $\Delta\theta_v$ in the top part of the downslope flows. The combination of these two effects results in $\gamma < 0$. It is interesting to note that the return flows are restricted to the part of the slope below $z_{HL\downarrow}$.

The mass flux from the downslope flows at the slope point corresponding to $z_{HL\downarrow}$ can be accumulated over time and compared to the mass in the volume of atmosphere beneath $z_{HL\downarrow}$, obtained using a Cartesian coordinate system. The resolution of the regular grid was 5 m, which was justified by Burns and Chemel (2014). Figure 4c shows that the mass within the CAP$_h$ below $z_{HL\downarrow}$ (m_a), is approximately equal to the accumulated mass from the downslope flows (m_b). The downslope flow mass flux was assumed to be symmetric about the valley axis. It was noted in Sect. 3.1 that $z_{HL\downarrow}$ is likely to be an under-estimation of the height of the humid layer close to the slopes, and so the point used to estimate the mass flux is likely to be slightly within the region of relatively dry air. Mass may be mixed into this region before reaching the mass flux point, and some slight under-estimation of the accumulation of mass from the downslope flows might be expected. Volumes V_a and V_b in Fig. 4c, calculated in

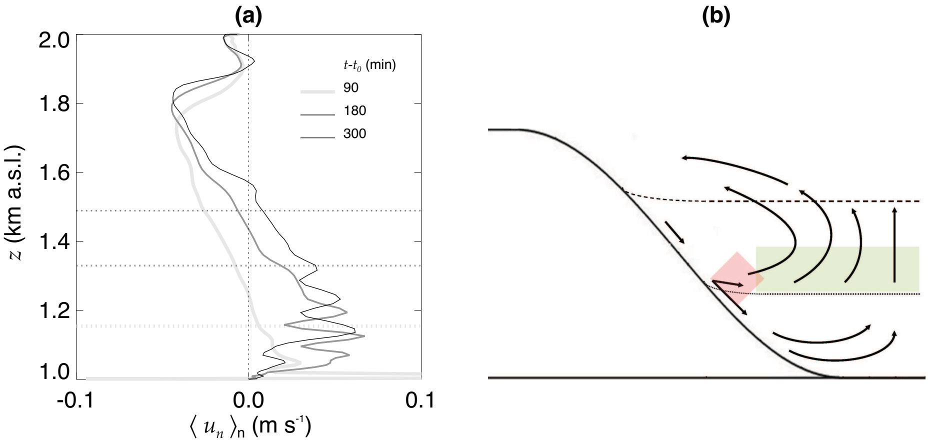

Fig. 5 **(a)** Variation of $\langle u_n \rangle_n$ along the western slope at three times, as indicated. Horizontal dotted-lines mark the height of $z_{HL\downarrow}$ at the three times ($z_{HL\downarrow}$ increases with time), and **(b)** a schematic illustrating the mechanisms that 'accelerate' the cooling in the upper portion of the valley atmosphere after $t = 180$ min. Arrows indicate flow direction, the dotted and dashed lines represent $z_{HL\downarrow}$ and $z_{CI\downarrow}$, respectively. The transparent red square and green rectangle indicate regions of enhanced mixing/detrainment and longwave radiative divergence, respectively. The latter corresponds to a region of relatively moist air.

a similar manner as m_a and m_b, demonstrate that the fluid is approximately incompressible. This analysis shows that q_v is an effective tracer of the flow field. Between $t = 60$ and 180 min $z_{HL\downarrow}$ is a reasonable estimate of the CAP$_h$ top height and so Fig. 4c confirms that the growth of the CAP$_h$ during this period is almost entirely due to the flux of mass from the downslope flows into the CAP$_h$. After $t \approx 180$ min the development of the CAP$_h$ is more complex and it is not possible to state that the upward expansion of the CAP$_h$ is essentially due to the flux of mass from the downslope flows into the CAP$_h$ (see Sect. 3.3.2).

It seems reasonable to suggest that a significant along-valley flow is likely to remove cooled air from the bottom of the valley and transport it to relatively flat regions (e.g. a plain). This is likely to reduce the speed of expansion of the CAP$_h$ as well as its maximum height, however, this needs to be confirmed by future research.

3.3.2 Development of the region of enhanced cooling

The gradual erosion of the CI is essentially caused by the interactions of the downslope flows with the expanding CAP$_h$, which forces the downslope flows back up the valley slopes, but is mixed and eroded as it does so. Relatively intense mixing occurs below the front of the downslope flow maximum region. Further mixing occurs across the regions of high-curvature associated with larger-scale circulations (see Fig. 3b and 3d). Although the streamlines indicate a flow across the CI (away from the slopes), at $t = 120$ min (when the CI height range approximates that of the HL), Sect. 3.3.1 demonstrated that any such flow must be small. The valley atmosphere dynamics are largely partitioned into two volumes, defined by $z_{HL\downarrow}$.

It appears that the erosion of the CI is accelerated as it comes into contact with the most energetic part of the flow (close to analysis points S_5 and S_6, compare Fig. 2a and 2b), and is broken up soon after $t = 180$ min. Between $t \approx 180$ and 300 min the top of the CAP$_h$ is difficult to define. $z_{HL\downarrow}$ does not always correspond to the CI or to the CAP$_h$ top height after $t = 180$ min. This suggests a rapid near-vertical transfer of heat energy, starting close to $t = 180$ min, between the CAP$_h$ (the top of which is reasonably estimated by $z_{HL\downarrow}$ at $t = 180$ min), and the atmosphere above $z_{HL\downarrow}$. This process corresponds well with the analysis of bulk cooling trends (see Sect. 3.4).

Vertical motions are initially restricted by the narrow region of near-horizontal flows close to the plateaux height, as well as the UML immediately below it. The latter region contributes to the development of an elevated inversion several hundred meters deep, extending below the UML, which restricts vertical motions further. Detrainment of air above $z_{HL\downarrow}$ is likely to converge close to the valley axis causing rising motions which will cool the atmosphere adiabatically. Air parcels will be forced laterally on reaching the elevated inversion, before being entrained into the downslope flows. This process is likely to be enhanced as the detrainment of fluid increases (see Fig. 5a). Air flows below $z_{HL\downarrow}$ and above $z_{CI\downarrow}$ generally do not have such a strong vertical component reducing cooling by adiabatic expansion. This is therefore another likely process that blurs the difference between the cooling of the lower and upper valley atmosphere, making it difficult to define the top of the CAP$_h$ between $t \approx 180$ and 300 min.

The elevated inversion also partially traps the layer of relatively high-q_v air beneath it ($z_{HL\uparrow}$ converges with $z_{CI\downarrow}$ towards the end of the simulation). The early development of the CAP$_h$ concentrates the available water vapour into the top portion of the valley atmosphere. A greater amount of water vapour in the atmosphere increases the bulk radiative cooling (Hoch et al. 2011). This is therefore another process that reduces the difference in cooling between the lower and upper valley atmosphere. A schematic is provided in Fig. 5b that summarizes the three identified processes that contribute to a more gradual variation of $\Delta\theta_v$ with height.

Several processes may contribute to the development of the elevated inversion. The vortices in the UML generally transport lower-θ_v air upwards and higher-θ_v air downwards, which tends to increase γ above and below the vortices. The circulation above $z_{HL\downarrow}$ generally transports relatively low-θ_v air into this region of the atmosphere from below. Radiative cooling decreases with z (not shown) as expected from Stefan's Law, mainly due to decreasing T with z, resulting in radiative divergence and increasing stratification.

A discontinuity in $z_{CI\downarrow}$ and $z_{CI\uparrow}$ occurs at $t \approx 250$ min. This is due to the destruction of the regions of relatively large γ lower in the valley atmosphere, and the establishment of the elevated inversion. Close to $t = 240$ min it becomes possible to identify a reasonably well defined decrease in $\langle\Delta\theta_v\rangle_y$ close to the top of the valley atmosphere, and by $t = 300$ min it is clear that the top of the CAP$_h$ corresponds well with $z_{CI\downarrow}$. The CAP$_h$ expands up to the bottom of the elevated inversion by the end of the simulation (i.e. 81 % of the valley depth).

After $t \approx 270$ min the change of $\max\left(\langle u_s\rangle_n\right)$ and $\max\left(u_{s,j}\right)$ are less sensitive to the change in $z_{HL\downarrow}$ (see Fig. 4b) and closer to the change in $z_{CI\downarrow}$ (see Fig. 2a), a better estimate of the CAP$_h$ top height during this period. The two maximum quantities generally lie somewhere between the two heights. Interestingly the height of $\max\left(\langle u_s\rangle_n\right)$ is generally less than $\max\left(u_{s,j}\right)$ after $t = 180$ min, which corresponds to the time of interaction between the CAP$_h$ and the most energetic region of the downslope flows. Both quantities lie above the height where $F_b \approx 0$. It seems that although there is flow penetration well below the height of $F_b \approx 0$ (see Fig. 3), the most energetic part of the flow is always above this level.

Figure 4b shows that $\max\left(n_{df}\right)$ is generally less than $\max\left(\langle u_s\rangle_n\right)$ and $\max\left(u_{s,j}\right)$, but has a similar trend. The algorithm used to compute $\max\left(n_{df}\right)$ avoided finding points towards the bottom of the slope, not far above z_{GBI}. Large values of n_{df} occur in this region where the downslope flows detrain above z_{GBI}. The algorithm considers the downslope flow before it is disrupted towards the base of the slope. A minimum point occurs in n_{df} towards the top of the slope (corresponding to a region of minimum entrainment or slight detrainment within the elevated inversion). This allowed max $\left(n_{df}\right)$ to be found by first moving along s whilst $n_{df}(s+1) < n_{df}(s)$ and then continuing along s whilst $n_{df}(s+1) > n_{df}(s)$. The algorithm shows an increase of n_{df} from the top of the slope. Figure 4b shows that max (n_j) is generally not sensitive to the CAP$_h$. max (n_j) was found by searching above z_{GBI} in order to avoid the bottom of the slope where n_j is not always well defined.

The decrease of $\langle u_s \rangle_n$ at points S_5 to S_8 compares well to the above analysis. At points S_8 and S_7 the decrease of $\langle u_s \rangle_n$ corresponds to either the rise of $z_{HL\downarrow}$ or $z_{CI\downarrow}$ (when the two heights are very similar). At point S_6 the more rapid decrease of $\langle u_s \rangle_n$ after $t = 190$ min corresponds to the rise of $z_{HL\downarrow}$. This occurs when the CI has already been eroded but largely before the rapid vertical transfers of heat energy, when $z_{HL\downarrow}$ still gives a reasonable estimate of the CAP$_h$ top height. The accelerated decrease of $\langle u_s \rangle_n$ at point S_5 appears to precede the arrival of $z_{HL\downarrow}$ (by about one hour), presumably due to the rapid vertical transfer of heat energy. It was noted in Sect. 3.2 that the curve for $\langle u_s \rangle_n$ at S_5 does not follow the general trends before $t = 180$ min. This indicates that without the development of the CAP$_h$ the region of the most energetic flows lies below the inflection point.

The main spatial and temporal variations of $\langle u_s \rangle_n$, illustrated in Fig. 2b, generally match those of the layer-averaged diabatic cooling $\langle L_c \rangle_{yn} = \partial \langle \theta_v \rangle_{yn} / \partial t + \langle u_s \rangle_n \partial \langle \theta_v \rangle_{yn} / \partial s$ (see Fig. 4d). As the CAP$_h$ engulfs a slope point the fluid in the downslope flow is brought closer to a thermal equilibrium with its environment, that is, the driving buoyancy force of the downslope flows F_b is reduced or nearly vanishes, and in some cases $F_b < 0$ (see below).

3.3.3 Downslope flow momentum budget and internal variability

Figure 6 displays time series of the components F_i of the layer-averaged downslope flow momentum balance (for u_s), from the Eulerian perspective, using y-averaged fields, at slope points S_1 to S_8. The components F_i correspond to the momentum balance for an irrotational, Boussinesq fluid, that is Eq. 1,

$$\left\langle \frac{\partial u_s}{\partial t} = \overbrace{-u_s \frac{\partial u_s}{\partial s}}^{F_{adv-s}} \overbrace{-u_n \frac{\partial u_s}{\partial n}}^{F_{adv-n}} \overbrace{-\frac{1}{\rho_r} \frac{\partial p'}{\partial s}}^{F_p} + \overbrace{g \frac{\theta_v'}{\theta_{v_a}} \sin\alpha}^{F_b} \overbrace{-\frac{\partial \tau_{sj}}{\partial X_j}}^{F_f} \right\rangle_n , \tag{1}$$

which includes along-slope and slope-normal advection F_{adv-s} and F_{adv-n}, respectively, the pressure force F_p, buoyancy force F_b, and subgrid-scale diffusion, denoted by F_f. Note that if the fields are not y-averaged it is possible to consider advection along y (F_{adv-v}), however, this term has no significant effect on the budget. p' is the perturbation pressure field, computed after applying $\langle\ \rangle_{xy}$ to the full pressure field p, where the averaging operator is that used in Sect. 3.1. τ_{sj} is the subgrid-scale stress tensor expressed using summation notation, where the index $j = \{s, n\}$, with $X_s \equiv s$, $X_n \equiv n$.

Figure 6 quantifies the influence of the CAP$_h$ on the downslope flows. F_b is shown to nearly vanish or to change to a negative force at slope points S_5 to S_8. The times of these events correspond almost exactly to the arrival of $z_{HL\downarrow}$ at each point (shown by a vertical dashed line). $z_{HL\downarrow}$ does not reach the slope points above S_5, and F_b remains significantly above zero at these positions. There is some reduction of F_b at all points; the degree of this reduction generally decreases with height, reflecting the decreasing influence of the CAP$_h$ with altitude. As expected there is a close correlation between F_b, $\langle L_c \rangle_{yn}$ and $\langle u_s \rangle_n$ (see also end of the previous section).

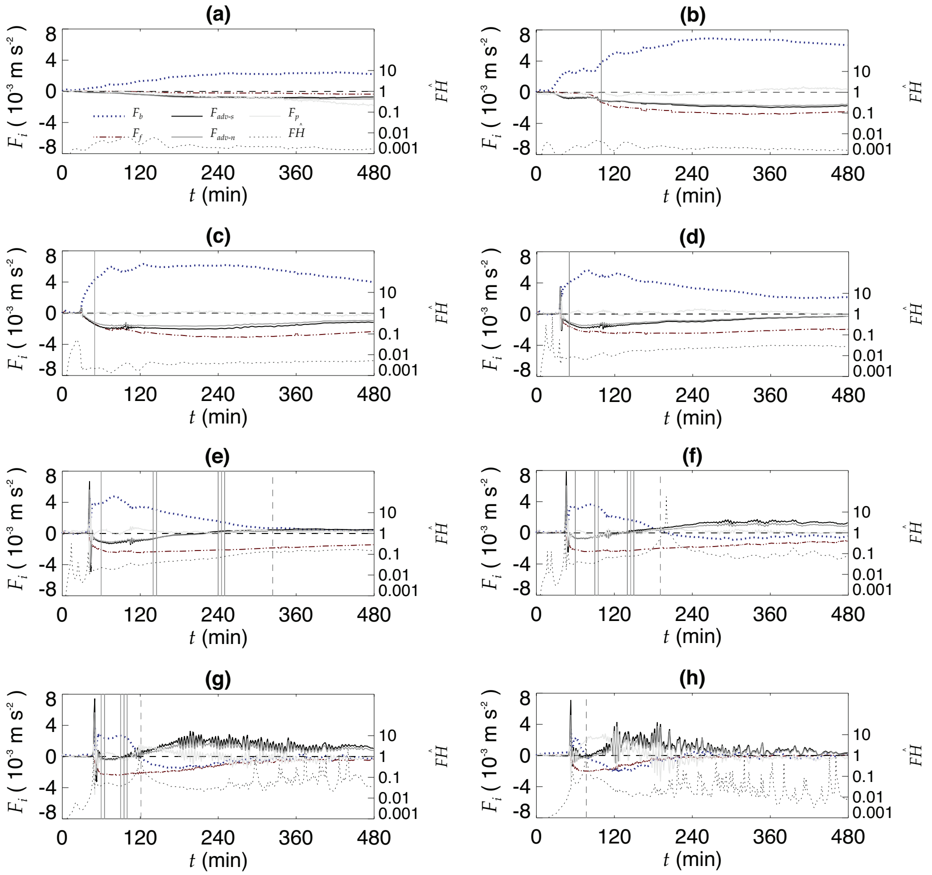

Fig. 6 Time series **(a)** to **(h)** of the components F_i of the layer-averaged downslope flow momentum balance (for u_s), using y-averaged fields, from the Eulerian perspective, at slope points S_1 to S_8, respectively. The analysis points were defined in Fig. 1. F_i corresponds to the momentum budget for an irrotational, Boussinesq fluid, and includes the buoyancy force F_b, subgrid-scale diffusion F_f, along-slope and slope-normal advection F_{adv-s} and F_{adv-n}, respectively, and the pressure force F_p. A black dashed horizontal line marks the zero level. The grey dashed vertical lines mark the arrival times of $z_{HL\downarrow}$. Solid grey vertical lines partition the flow into different regimes; one line marks the start of the shooting flow regime, two lines mark the end of this regime and the start of the near-equilibrium flow regime, which ends with the occurrence of three lines. The modified Froude number $F\hat{H}$ is over-plotted for comparison [see Mahrt (1982) and the text for details].

Figures 6b to 6f (slope points S_2 to S_8) show time periods where there is an approximate balance between F_b, $F_{adv} = F_{adv-s} + F_{adv-n}$ and F_f. The approximate start and end times of these periods are marked by single solid vertical lines and two solid vertical lines, respectively. Downslope flows resulting from a balance between F_b, F_{adv-s} and F_f were classified as 'shooting flows' by Mahrt (1982). F_{adv-n} cannot be neglected for the system considered by this work; the fluid normal to the slope is not in hydrostatic balance, a condition that presumably would require a more gentle slope. The occurrence of two solid vertical lines marks the beginning of a period where there is an approximate balance between F_b and F_f, classified by Mahrt (1982) as 'near-equilibrium flows'. The approximate end of such a period is marked by a set of three vertical solid lines. Note that there is a short period of near-equilibrium flows at S_8 and a near-equilibrium flow regime is reached by the end of the simulation at S_4, however, in both cases the vertical lines were omitted for clarity.

There is therefore a transition from shooting flows to near-equilibrium flows at slope positions reached by $z_{HL\downarrow}$, with a more rapid evolution of the flow occurring with distance down the slope. After $z_{HL\downarrow}$ reaches a slope point F_{adv-s} generally changes to a positive force. This reflects the fact that the region of maximum downslope flows retreats back up the western slope ahead of $z_{HL\downarrow}$; the maximum region of the downslope flows becomes a source of momentum for points below it. F_{adv-n} follows F_{adv-s}; a convergence of fluid along the slope (i.e., $F_{adv-s} > 0$) must result in detrainment given that the fluid is approximately incompressible (see Sect. 3.3.1). The correspondence between flow convergence along s and detrainment is confirmed by a comparison of Fig. 2b and Fig. 5a. $\langle \partial u_s / \partial n \rangle_n < 0$ (not shown), due to the typical profile of the downslope flows, more specifically the close proximity of the cold-air jet to the ground surface. Therefore the two advection terms tend to follow one another. Detrainment below $z_{HL\downarrow}$ is presumably aided by $F_b < 0$ in this region.

The modified Froude number $F\hat{H}$ (Mahrt 1982) has been over-plotted for comparison, where $F = U^2/(g'H)$ is the Froude number. U and H are the speed and depth scales of the downslope flow, set to $\langle u_s \rangle_n$ and n_{df}, respectively. $g' = g\,\delta\theta_v/\theta_{v_a}$ is the 'reduced gravity', where $\delta\theta_v$ is the temperature deficit scale of the flow; g' was extracted from F_b. The non-dimensional height $\hat{H} = H/\Delta Z_s$, where ΔZ_s is the height change made by the slope ($\hat{H} \ll 1$ here). As expected $F\hat{H} < 1$ for both the shooting-flow and equilibrium-flow regimes. $F\hat{H}$ generally increases down the slope, with values of $F\hat{H} = \mathcal{O}(1)$ occurring at times when either $F_b \approx 0$ and $F_{adv} \neq 0$, or when $F_b \approx F_{adv}$ when the budget is not dominated by the two terms.

Small time variations can be seen on most of the curves of Fig. 2b. A fast Fourier transform has been used to investigate these variations further. It is not possible to apply the spectral analysis to $\langle u_s \rangle_n$ since the averaging along y distorts the true flow variations. Instead the spectral analysis was applied to $\langle \tilde{u}_s \rangle_n$, where $\tilde{u}_s$ was derived from u and w taken halfway along y. The general trends in $\langle \tilde{u}_s \rangle_n$ are the same as those in $\langle u_s \rangle_n$, however, there are significant differences in the amplitude of the variations (see Fig. 7a). Figure 7a shows $\langle \tilde{u}_s \rangle_n$ for slope points S_5 to S_7 and demonstrates that the expanding CAP$_h$ induces relatively large variations in $\langle \tilde{u}_s \rangle_n$ as it reaches each point. The arrival time of $z_{HL\downarrow}$ is marked by concentric circles, which correspond to $t = 121$, 191 and 324 min, respectively ($z_{HL\downarrow}$ increases with time). Some negative values of $\langle \tilde{u}_s \rangle_n$ occur for point S_7 at times when the downslope flows are not well defined due to their interactions with the dense air towards the valley floor. Note that the variations in $\langle \tilde{u}_s \rangle_n$ are very similar to those in $\langle u_s \rangle_n$ above S_5. Below S_7 $\langle \tilde{u}_s \rangle_n$ and $\langle u_s \rangle_n$ become increasingly variable.

Close inspection of Fig. 7a reveals that the variations have a frequency in the range of approximately 0.002 to 0.005 rad s^{-1} (i.e., a period in the range of 20 to 50 min). Figure 7b to Fig. 7l show the spectra of $\langle \tilde{u}_s \rangle_n$ for analysis points S_1 to F_2. An analysis of these spectra reveals that the range of frequencies evident in Fig. 7a clearly dominates the spectrum at points S_4 to S_8, if the frequencies below 0.002 rad s^{-1} (due to longer-term trends) are disregarded. Above S_4 and below S_8 it is harder to see this effect. Peaks close to 0.002 rad s^{-1} above S_4 are due to variations that occur during the establishment of the flow, which takes longer in this region of the slope (see Fig. 2b). It is clear that it is not possible to find a single dominant frequency. It is possible that the type of oscillations predicted by McNider (1982) contribute to the dominant range of frequencies identified above, however, it is difficult to confirm this. The assumptions made to arrive at the model derived by McNider (1982) are generally not valid for the flow system considered by this work. There are other candidates that may cause variations in the downslope flow. There is high shear where the flow

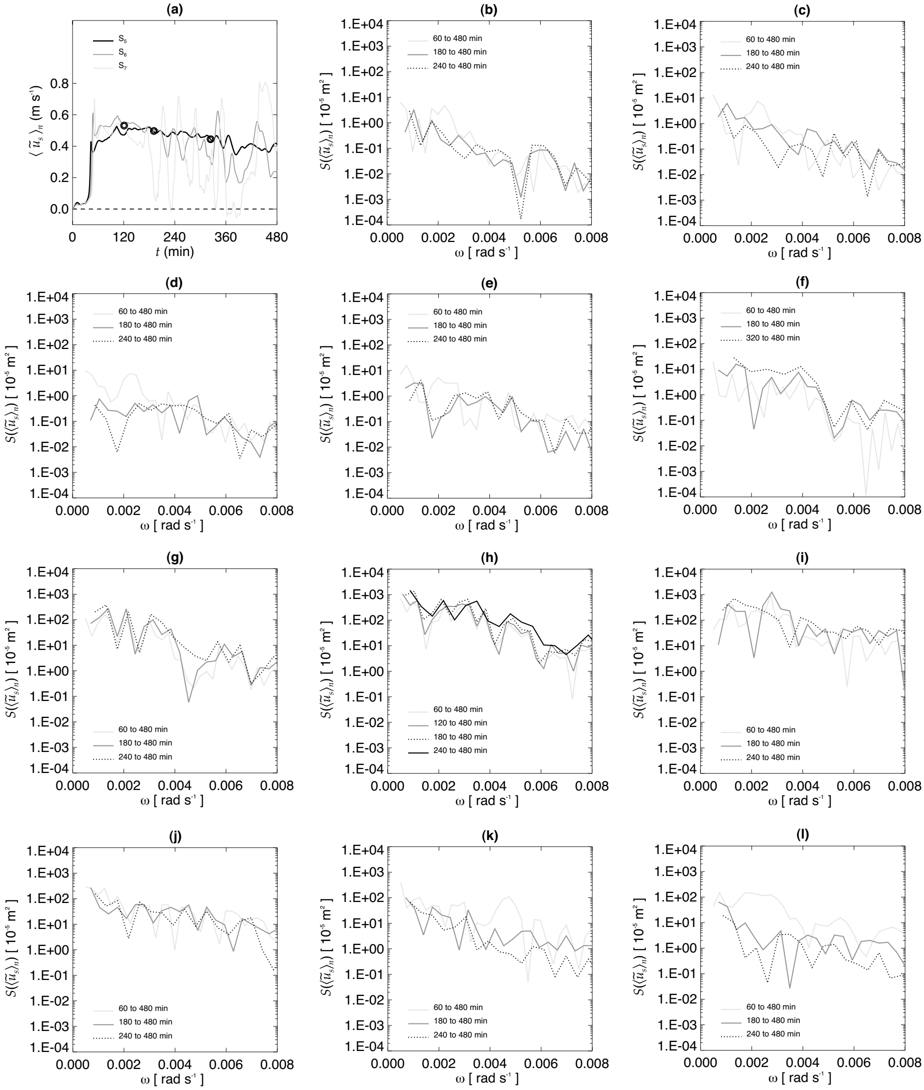

Fig. 7 **(a)** Time series of the layer-averaged downslope flows $\langle \tilde{u}_s \rangle_n$ at slope points S_5 to S_7. $\tilde{u}_s$ was derived from u and w taken halfway along y. The arrival times of $z_{HL\downarrow}$ are marked by concentric circles ($z_{HL\downarrow}$ increases with time). **(b)** to **(l)** Spectra of $\langle \tilde{u}_s \rangle_n$ at analysis points S_1 to F_2, respectively. The spectra were determined for different time periods to analyze the time variation of the spectra, which was limited by the resolution of the WRF model output (1 min).

springs back after over-shooting $F_b = 0$, which may cause Kelvin-Helmholtz (KH) instabilities. There is a region of unstable air below $z_{HL\downarrow}$ (see Sect. 3.3.1), which may also trigger KH instabilities. Interesting elongated features orientated downslope are evident in the flow below S_5 (see Fig. 8), which are approximately coincident with the region where there is a clear range of dominant frequencies, the region of high shear and where there exists a region of unstable air. Confirmation of the exact causes and nature of the variations found in $\langle \tilde{u}_s \rangle_n$

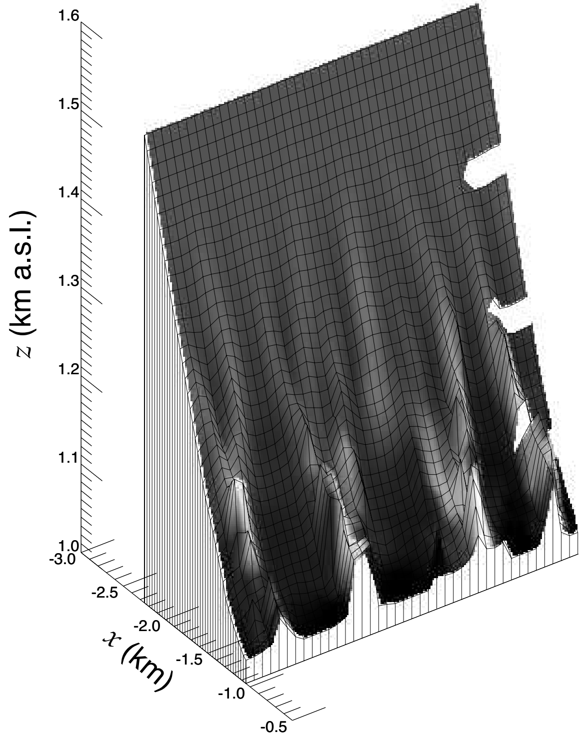

Fig. 8 Height of the downslope flow top surface at $t = 240$ min, between slope points S_5 and S_9 (defined in Fig. 1), where intermediate point heights are indicated by the notches on the right of the figure. Grid intersections indicate the horizontal grid resolution $\Delta x = \Delta y = 30$ m. The surface uses the full y-dimension that was given a length of 1.2 km. Shading is scaled by the depth of the downslope flows to help reveal the pattern.

is beyond the scope of this work but would make an interesting topic of future research. The variations in the flow may be formed from a combination of processes.

3.4 Bulk cooling mechanisms and atmospheric characteristics

The various heights defined in Sect. 3.1 enable the subdivision of the valley atmosphere into a number of volumes, shown in Fig. 2a. This provides one means of investigating the varying cooling mechanisms in different regions of the valley atmosphere. The volumes were allowed to encompass the full y-dimension and limited along x between the top of each slope (i.e. $-3.75 \le x \le 3.75$ km).

Figure 9a shows $\langle R_r \rangle_V / \langle R \rangle_V$, where R_r is the time-rate of change of θ_v ($\partial \theta_v / \partial t \equiv R$), due to radiation. The operator $\langle\ \rangle_V$ refers to a volume average across any of the defined volumes. Volume averages were computed by first applying $\langle\ \rangle_y$, before projecting the variables onto a linear orthogonal mesh with a resolution of 5 m, that filled the valley space. $\langle R_r \rangle_{V_1} / \langle R \rangle_{V_1}$ confirms that radiative effects generally dominate the instantaneous cooling within the GBI. Between $t \approx 30$ and 100 min instantaneous cooling from the dynamics (i.e., the combined effects of advection and subgrid-scale mixing) is dominant. After this time radiative divergence generally dominates the instantaneous cooling as the region of maximum downslope flows is forced away from the GBI. Figure 9b shows $\langle\Delta\theta_{v_r}\rangle_V/\langle\Delta\theta_v\rangle_V$, where $\Delta\theta_{v_r}$ is the change in temperature from $t=0$ due to radiative effects. $\langle\Delta\theta_{v_r}\rangle_{V_1}/\langle\Delta\theta_v\rangle_{V_1}$ remains close to 0.5 due to the dominance of instantaneous cooling by the dynamics when the temperature changes are close to their maximum (see Fig. 9c).

$\langle R_r\rangle_V/\langle R\rangle_V$ and $\langle\Delta\theta_{v_r}\rangle_V/\langle\Delta\theta_v\rangle_V$ for V_2 and V_3 confirm that the cooling is almost equally partitioned between radiative and dynamics effects within the CAP$_h$ and the elevated inversion. Figure 9b shows that $\langle\Delta\theta_{v_r}\rangle_{V_2}/\langle\Delta\theta_v\rangle_{V_2}$ is always less than 0.5 after approximately $t=85$ min. This explains the decrease of $\langle\Delta\theta_{v_r}/\Delta\theta_v\rangle_{va}$ over time found by Burns and Chemel (2014), where $\langle\ \rangle_{va}$ is an average across the full valley atmosphere.

After $t=300$ min, $z_{CI\downarrow}$ appears to be a more accurate measure of the CAP$_h$ top height, however, the effect of using $z_{HL\downarrow}$ in place of $z_{CI\downarrow}$ does not change the results qualitatively. The small difference decreases over time as $z_{HL\downarrow}$ moves closer to $z_{CI\downarrow}$. $\langle\Delta\theta_{v_r}\rangle_V/\langle\Delta\theta_v\rangle_V$ can be expected to lag behind $\langle R_r\rangle_V/\langle R\rangle_V$, which is evident in the data. Large variations in $\langle R_r\rangle_V/\langle R\rangle_V$ occur at varying times before $t=180$ min when these volumes are not well defined. It should be noted that some over-estimation of radiative cooling is likely to be present in the results, which rely on the use of a one-dimensional radiative transfer scheme (Hoch et al. 2011).

The partitioning of the accumulated temperature changes within the GBI and CAP$_h$, between radiative and dynamical effects, occurs largely within the first two hours of simulation. This corresponds to the time period of maximum instantaneous temperature changes (see Fig. 9c). This partitioning effect is also true for the full valley atmosphere (Burns and Chemel 2014).

The cooling within volumes V_4 to V_6 (see Fig. 9a and 9b), at the top of or above the valley atmosphere, is almost completely dominated by radiative effects. $\langle\Delta\theta_{v_r}\rangle_V/\langle\Delta\theta_v\rangle_V$ for V_4 and V_5 generally decrease over time, suggesting an interaction between the CAP$_h$ and the valley atmosphere above, and an interaction between the latter and the free atmosphere above the valley. As the CAP$_h$ expands higher the dynamics are able to increasingly cool air at greater elevations.

Figures 9c and 9d show the general reduction of cooling rates and accumulated temperature changes with height within and above the valley atmosphere. A minimum point in the time series of $|\langle R\rangle_{V_1}|$ (see Fig. 9c) occurs close to $t=100$ min when it falls below that of $|\langle R\rangle_{V_2}|$, which follows an initial peak in $|\langle R\rangle_{V_1}|$ close to $t=60$ min. $|\langle R\rangle_{V_1}|$ first peaks close to the arrival time of the region of maximum downslope flows. $|\langle R\rangle_{V_1}|$ then decreases rapidly during the time period when the region of maximum downslope flows displaces the GBI vertically, reducing its intensity by advective and mixing processes (Sect. 3.3.1). This reduction in intensity follows the reduction in average atmospheric stability (see Fig. 9e). The advection and mixing of higher-θ_v air from above reduces $|\langle R\rangle_{V_1}|$. As the region of maximum downslope flows is forced back up the valley slopes (see Fig. 4b) $|\langle R\rangle_{V_1}|$ and $\langle\gamma\rangle_{V_1}$ increase once again. The absolute magnitude of $\langle R\rangle_V$ for V_1 to V_3 are shown to nearly converge by the end of the simulation (see Fig. 9c) indicating that these regions tend towards a state of thermal equilibrium with one another. The average accumulated temperature change within the GBI is close to double the change within the rest of the valley atmosphere, which cools by about twice as much as the free atmosphere above.

Careful inspection of Figure 9d reveals a slight reduction in the rate of increase of $|\langle\Delta\theta_v\rangle_{V_2}|$ after $t\approx 180$ min. Fig. 9c shows the average cooling rate in V_2 to approximate that of V_3 by $t\approx 240$ min and to fall below the cooling rate of V_3 by $t\approx 300$ min. These bulk features correspond very well to the details discussed in Sect. 3.3.2.

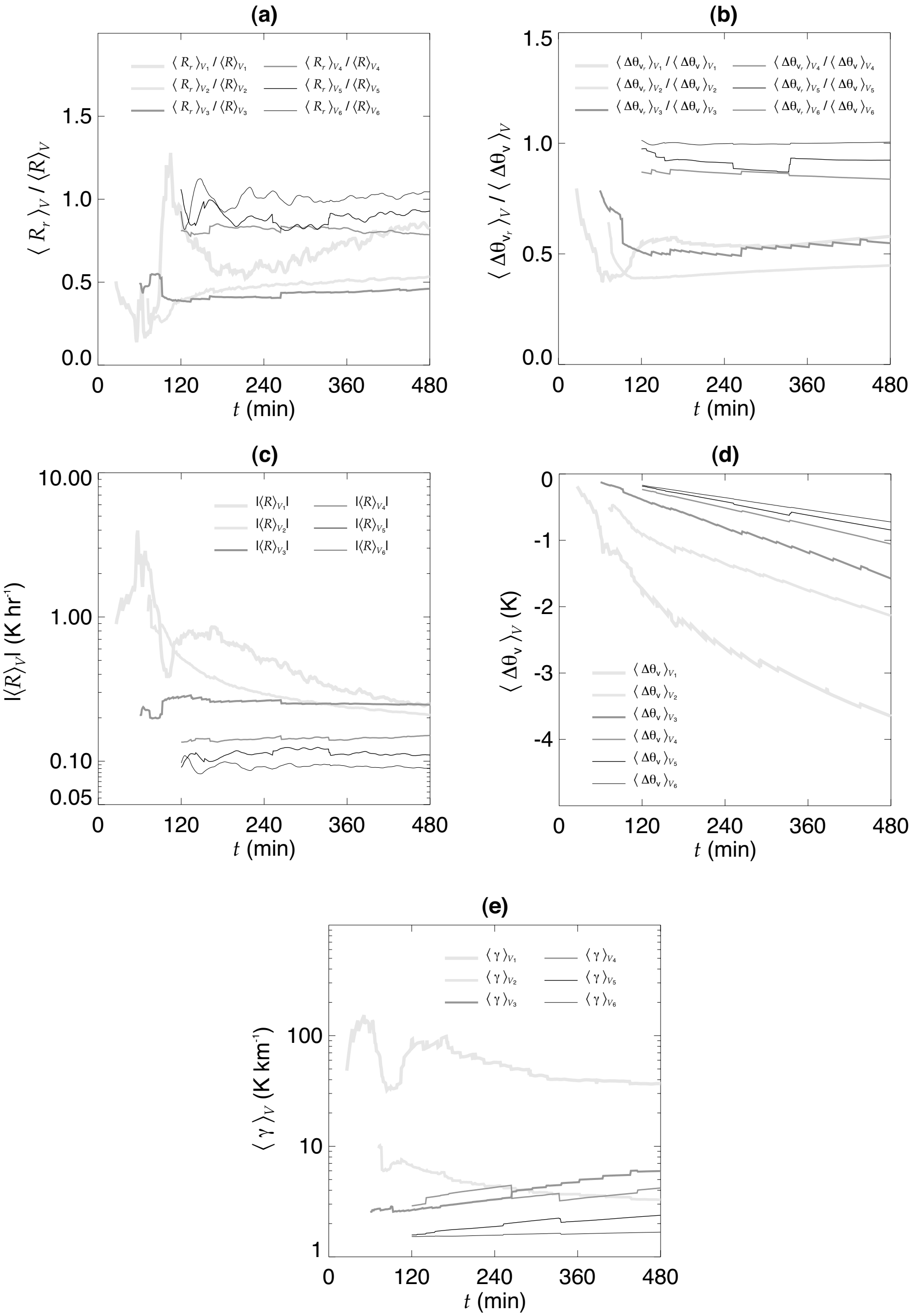

Fig. 9 Time series of volume averages for V_1 to V_6 (defined in Fig. 2a) of **(a)** $\langle R_r \rangle_V / \langle R \rangle_V$, where R_r is the time-rate of change of virtual potential temperature ($\partial\theta_v/\partial t \equiv R$) due to radiation, **(b)** $\langle \Delta\theta_{v_r} \rangle_V / \langle \Delta\theta_v \rangle_V$, where $\Delta\theta_{v_r}$ is the accumulated change of virtual potential temperature ($\Delta\theta_v$) due to radiation, **(c)** the absolute magnitude of R, where $\langle R \rangle_v < 0$, **(d)** $\Delta\theta_v$, and **(e)** $\gamma \equiv \partial\theta_v/\partial z$.

Figure 9e shows that the atmospheric stability of all the defined regions is larger than γ_0 at the end of the simulation. For example, on average, $\gamma \approx 25\,\gamma_0$, $2\,\gamma_0$ and $4\,\gamma_0$ within the GBI, CAP_h and elevated inversion, respectively, by the end of the simulation. The average atmospheric stability of the GBI is approximately an order of magnitude greater than the majority of the rest of the valley atmosphere, or the free atmosphere above, with the exception of the elevated inversion after $t \approx 300$ min. The average stability of both the GBI and CAP_h are shown to decrease after $t \approx 120$ min, which is in-line with the observations of Neff and King (1989).

$\langle\gamma\rangle_{V_3}$ is shown to increase more rapidly than $\langle\gamma\rangle_{V_4}$, whilst $\langle\gamma\rangle_{V_2}$ decreases, which quantifies the development of the elevated inversion and the UML. $\langle\gamma\rangle_{V_5}$ increases at a greater rate than $\langle\gamma\rangle_{V_6}$ quantifying the development of the USL. Close to $t = 240$ min, $\langle\gamma\rangle_{V_2}$ falls below $\langle\gamma\rangle_{V_3}$, which corresponds to the destruction of the lower layers of relatively large γ and the establishment of the elevated inversion, discussed in Sect. 3.3.2.

4 Summary

A numerical model has been used to characterize the development of a region of enhanced cooling and some of its interactions with downslope flows, in an idealized alpine valley with a width of order 10 km, under decoupled stable conditions.

After the initial intensification of the downslope flows, a region of enhanced cooling was found to expand up through the valley atmosphere. Initially this expansion is fairly gradual and almost entirely due to the flux of mass into the region from the downslope flows. The region is relatively dry with a capping inversion at its top, defined by variable mixing. A layer of moist air is carried above the region and concentrated into the top half of the valley atmosphere.

The downslope flows first displace the ground-based inversion vertically and weaken it before the region of enhanced cooling forces the most energetic region of the downslope flows back up the valley slopes, which initially erodes away the top of the ground-based inversion.

The growth of the region of enhanced cooling is accelerated when the expanding region encounters the most energetic part of the downslope flows some 2 h after sunset. This results in enhanced mixing close to the top of the region of enhanced cooling, the final destruction of the initial capping inversion, and a relatively rapid near-vertical transfer of heat energy. From 2 h after sunset the region of enhanced cooling does not essentially expand due to the flux of mass into the dry region of air.

A region of near-horizontal streamlines lies above a layer of vortices close to the top of the valley atmosphere. The latter directly contributes to the development of an elevated inversion. This elevated inversion is also likely formed by the transport of low-potential temperature air from below and by radiative divergence. These features at the top of the atmosphere partially trap air flows within the valley atmosphere. These valley-atmosphere flows are largely partitioned between two volumes, defined by the top of the region of relatively dry air. The expanding region of dry air concentrates the available water vapour into the upper part of the valley atmosphere, increasing the cooling there due to radiative processes. At the same time the re-circulation of air above the region of dry air is intensified causing enhanced adiabatic cooling. Therefore, there appear to be three key processes that blur the difference in cooling between the upper and lower parts of the valley atmosphere. These processes make it difficult to define the top of the region of enhanced cooling between 2 and 4 h after sunset.

Generally entrainment of air into the slope flows occurs above the region of dry air and detrainment of air from the downslope flows occurs below the top of this region. The detrainment of air appears to be caused by several processes. The flows will tend to leave the slope close to their level of neutral buoyancy. Detrainment is enhanced by shear-induced mixing in the region where the flows ‘spring-back’ after ‘over-shooting’ their level of neutral buoyancy, a characteristic of gravity currents in the ‘plume regime’. Return flows occur where the flows spring-back and are restricted to the region of dry air. The downslope flows are deflected above the ground-based inversion, which is generally an order of magnitude more stable than the atmosphere above it (except for the elevated inversion after 4 h following sunset). An analysis of the detrainment of air from the downslope flows reveals a layering effect that will generate shears and mixing within the region of enhanced cooling. The return flows help to create a region of unstable air above the downslope flows by transporting low potential temperature air from below. At the same time the downslope flows advect high potential temperature air downslope causing warmer temperatures in the top part of the downslope flows less affected by the cooling ground surface.

As the CAP_h engulfs the slopes, the downslope flows mix with it, reducing their negative buoyancy, causing them to slow down. With a lower temperature deficit the ability of the downslope flows to lose thermal energy to the sloping surface is reduced. A significant increase and decrease of the downslope flow speeds occurs over time for slope points engulfed by the region of dry air. From 2 h after sunset the downslope flow speeds generally increase from the top of the slopes towards the slope inflection points, and decrease after this point towards the valley floor. The flow field before 2 h after sunset reveals that, without the influence of the region of enhanced cooling, the maximum region of the downslope flows is below the slope inflection points. There is a transition from shooting flows to near-equilibrium flows at slope points reached by the region of dry air, with a more rapid evolution of the flow occurring with distance down the slope. The expansion of the region of enhanced cooling increases the height of the maximum downslope flow depth.

The expanding region of enhanced cooling has been found to initiate relatively large variations of the downslope flows with periods ranging between approximately 20 and 50 min. Disregarding variations due to longer-term flow changes, this range of periods has been found to dominate the spectra of the downslope flows engulfed by the region of dry air, away from the bottom of the slope. The exact nature and causes of these flow variations remains unclear. These flow variations are approximately coincident with a region of high shear, a region of unstable air, and a region of elongated flow features orientated downslope.

After the initial intensification of the downslope flows, the instantaneous cooling in the ground-based inversion is generally dominated by radiative effects. This occurs as the maximum region of the downslope flows is forced further away from the ground-based inversion. The normalized temperature changes within the ground-based inversion remain close to 0.5 due to the initial dominance of cooling from the dynamics when temperature changes are close to their maximum. The cooling within the region of enhanced cooling and within the elevated inversion is almost equally partitioned between radiative and dynamics effects. The partitioning of the cooling between the two processes occurs largely within an hour following sunset.

The cooling at the top of or above the valley atmosphere is almost completely dominated by radiative effects, but with generally an increasing contribution to the cooling by the dynamics. This suggests some interaction between the valley atmosphere and the free atmosphere above, as the region of enhanced cooling evolves.

The average temperature changes within the ground-based inversion are approximately double those of the rest of the valley atmosphere, which cools by about twice as much as the free atmosphere above. The three lowest volumes tend towards a state of thermal equilibrium with one another by the end of the simulation, however, at this time they are not in a state of thermal equilibrium with their external environment.

The average atmospheric stability of all defined volumes is greater than the initial atmospheric stability at the start of the simulation. The final stability within the ground-based inversion, the region of enhanced cooling and the elevated inversion is close to 25, 2 and 4 times the initial atmospheric stability, respectively. The stability of the ground-based inversion and the region of enhanced cooling decreases after approximately an hour following sunset.

It should be stated that these results are for a particular valley geometry, and set of initial and boundary conditions. A future sensitivity study should test the generality of these results.

References

Acevedo OC, Fitzjarrald DR (2001) The early evening surface-layer transition: Temporal and spatial variability. J Atmos Sci 58:2650–2667

Anquetin S, Guilbaud C, Chollet JP (1999) Thermal valley inversion impact on the dispersion of a passive pollutant in a complex mountainous area. Atmos Environ 33:3953–3959

Baines PG (2008) Mixing in downslope flows in the ocean-plumes versus gravity currents. Atmos Ocean 46:405–419

Blyth S, Groombridge B, Lysenko I, Miles L, Newton A (2002) Mountain Watch: Environmental change and sustainable development in mountains. Report, UNEP World Conservation Monitoring Centre, Cambridge, UK, 80 pp

Brulfert C, Chemel C, Chaxel E, Chollet JP (2005) Modelling photochemistry in alpine valleys. Atmos Chem Phys 5:2341–2355

Burns P, Chemel C (2014) Evolution of cold-air-pooling processes in complex terrain. Boundary-Layer Meteorol 150:423–447.

Catalano F, Cenedese A (2010) High-resolution numerical modeling of thermally driven slope winds in a valley with strong capping. J Appl Meteorol Climatol 49:1859–1880

Chazette P, Couvert P, Randriamiarisoa H, Sanak J, Bonsang B, Moral P, Berthier S, Salanave S, Toussaint F (2005) Three-dimensional survey of pollution during winter in French Alps valleys. Atmos Environ 39:1035–1047

Chemel C, Burns P (2013) Pollutant dispersion in a developing valley cold-air pool. Boundary-Layer Meteorol Submitted

Chen F, Dudhia J (2001) Coupling an advanced land-surface/hydrology model with the Penn State/NCAR MM5 modeling system. Part I: model implementation and sensitivity. Mon Weather Rev 129:569–585

Daly C, Conklin DR, Unsworth MH (2010) Local atmospheric decoupling in complex topography alters climate change impacts. Int J Climatol 30:1857–1864

Deardorff JW (1980) Stratocumulus-capped mixed layers derived from a three-dimensional model. Boundary-Layer Meteorol 18:495–527

Dudhia J (1989) Numerical study of convection observed during the winter monsoon experiment using a mesoscale two-dimensional model. J Atmos Sci 46:3077–3107

Dudhia J (1995) Reply. Mon Weather Rev 123:2573–2575

Fleagle RG (1950) A theory of air drainage. J Meteorol 7:227–232

Gustavsson T, Karlsson M, Bogren J, Lindqvist S (1998) Development of temperature patterns during clear nights. J Appl Meteorol 37:559–571

Hoch SW, Whiteman DC, Mayer B (2011) A systematic study of longwave radiative heating and cooling within valleys and basins using a three-dimensional radiative transfer model. J Appl Meteorol Climatol 50:2473–2489

Iacono MJ, Delamere JS, Mlawer EJ, Shephard MW, Clough SA, Collins WD (2008) Radiative forcing by long-lived greenhouse gases: calculations with the AER radiative transfer models. J Geophys Res 113:D13,103, DOI 10.1029/2008JD009944

Jiménez PA, Dudhia J, Gonzalez-Rouco JF, Navarro J, Montávez JP, García-Bustamante E (2012) A revised scheme for the WRF surface layer formulation. Mon Weather Rev 140:898–918

Klemp JB, Dudhia J, Hassiotis AD (2008) An upper gravity-wave absorbing layer for NWP applications. Mon Weather Rev 136:3987–4004

Largeron Y, Staquet C, Chemel C (2013) Characterization of oscillatory motions in the stable atmosphere of a deep valley. Boundary-Layer Meteorol 148:439–454

Mahrt L (1982) Momentum balance of gravity flows. J Atmos Sci 39:2701–2711

Mahrt L (2014) Stably Stratified Atmospheric Boundary Layers. Ann. Rev. Fluid Mech., DOI 10.1146/annurev-fluid-010313-141354

Mahrt L, Vickers D, Nakamura R, Soler MR, Sun JL, Burns S, Lenschow DH (2001) Shallow drainage flows. Boundary-Layer Meteorol 101:243–260

Manins, PC, Sawford, BL (1979) A model of katabatic winds. J Atmos Sci 36:619–630

Mansell ER, Ziegler CL, Bruning EC (2010) Simulated electrification of a small thunderstorm with two-moment bulk microphysics. J Atmos Sci 67:171–194

Maybeck M, Green P, Vorosmarty C (2001) A new typology for mountains and other relief classes: An application to global continental water resources and population distribution. Mountain Research and Development 21:34–45

McNider RT (1982) A note on velocity fluctuations in drainage flows. J Atmos Sci 39:1658–1660

Moeng CH, Dudhia J, Klemp J, Sullivan P (2007) Examining two-way grid nesting for large eddy simulation of the PBL using the WRF model. Mon Weather Rev 135:2295–2311

Nachabe MH (1998) Refining the definition of field capacity in the literature. J Irrigat Drain Eng 124:230–232

Nadeau DF, Pardyjak ER, Higgins CW, Huwald H, Parlange MB (2012) Flow during the evening transition over steep Alpine slopes. Q J R Meteorol Soc, DOI :10.1002/qj.1985

Neff WD, King, CW (1989) The Accumulation and Pooling of Drainage Flows in a Large Basin. J Appl Meteorol 28:518–529

Noppel H, Fiedler F (2002) Mesoscale heat transport over complex terrain by slope winds – a conceptual model and numerical simulations. Boundary-Layer Meteorol 104:73–97

Oke TR (1987) Boundary Layer Climates. Routledge, London, UK, London, UK, 464 pp

Price JD, Vosper S, Brown A, Ross A, Clark P, Davies F, Horlacher V, Claxton B, McGregor JR, Hoare JS, Jemmett-Smith B, Sheridan P (2011) COLPEX: field and numerical studies over a region of small hills. Bull Am Meteorol Soc 92:1636–1650

Scotti A, Meneveau C, Lilly DK (1993) Generalized Smagorinsky model for anisotropic grids. Phys Fluids 5:2306–2308

Shu CW (2003) High-order finite difference and finite volume WENO schemes and discontinuous Galerkin methods for CFD. Int J Comput Fluid Dyn 17:107–118

Silcox GD, Kelly KE, Crosman ET, Whiteman CD, Allen BL (2012) Wintertime $PM_{2.5}$ concentrations during persistent, multi-day cold-air pools in a mountain valley. Atmos Environ 46:17–24

Skamarock WC, Klemp JB, Dudhia J, Gill DO, Barker DM, Duda MG, Huang XY, Wang W, Powers JG (2008) A Description of the Advanced Research WRF Version 3. NCAR Technical Note NCAR/TN-475+STR, NCAR, Boulder, CO, USA, 125 pp

Szintai B, Kaufmann P, Rotach MW (2010) Simulation of pollutant transport in complex terrain with a numerical weather prediction–particle dispersion model combination. Boundary-Layer Meteorol 137:373–396

Vergeiner I, Dreiseitl E (1987) Valley winds and slope winds – Observations and elementary thoughts. Meteorol Atmos Phys 36:264–286

Vinokur M (1980) On One-Dimensional Stretching Functions for Finite-Difference Calculations. NASA Contractor Report 3313, NASA, Washington, DC, USA, 56 pp

Whiteman CD (2000) Mountain Meteorology: fundamentals and applications. Oxford University Press, New York, NY, USA, 355 pp

Zardi D, Whiteman CD (2013) Diurnal mountain wind systems. In: Chow FK, De Wekker SFJ, Snyder BJ (eds) Mountain Weather Research and Forecasting: Recent Progress and Current Challenges, Springer Atmospheric Sciences, Springer, New York, NY, USA, chap 2, pp 35–119